Microchimica Acta (2020) 187:397
https://doi.org/10.1007/s00604-020-04367-8

ORIGINAL PAPER

Gold nanoparticle–modified black phosphorus nanosheets with improved stability for detection of circulating tumor cells

Shuping Liu[1] · Junjun Luo[1] · Xingxing Jiang[1] · Xiaoqing Li[1] · Minghui Yang[1]

Received: 6 March 2020 / Accepted: 1 June 2020

Abstract

Gold nanoparticle (AuNP)–anchored BP nanosheets were synthesized through in situ growth of AuNPs onto BP. Due to the strong chelating ability of P or phosphorus oxides with AuNPs, the stability of BP is improved. As proof-of-concept demonstration of the functionalized BP, electrochemical detection of circulating tumor cells (CTCs) based on BP@AuNPs@aptamer as a probe combined with immunomagnetic separation is reported. The aptamer can specifically bind with CTCs, while the phosphorus oxides including phosphite ion and phosphate ion (PxOy species) on BP and aptamer can react with molybdate to generate an electrochemical current, leading to dual signal amplification. The biosensor is applied to MCF-7 cell detection and displays good analytical performance with a detection limit of 2 cell mL^{-1}. Furthermore, the practicality of this biosensor was validated through sensitive determination of MCF-7 cells in human blood. Therefore, the reported biosensor could be applied to detect other biomarkers, offering an ultrasensitive strategy for clinical diagnostics.

Keywords BP nanosheets · Immunomagnetic separation · Circulating tumor cells · Gold nanoparticles · Electrochemical detection

Introduction

Cancer has aroused widespread concern because of its high mortality rate [1, 2]. It is well known that tumor metastasis is the main cause of death in cancer patients [3]. Preoperative diagnosis and detection of cancer cell metastasis from blood are particularly important in the treatment of cancer [4]. Circulating tumor cells (CTCs) acted as the biomarkers for tumor cell metastasis as they can flow into the bloodstream from the source of primary tumor sites [5, 6]. Currently, many methods have been developed to detect CTCs, including microfluid [7], fluorescence [8], flow cytometry [9], and electrochemistry [10]. Owing to its high sensitivity and simple instrumentation, electrochemical methods have significant advantages in cancer cell detection.

The number of CTCs in the peripheral blood of patient is extremely rare [11]. Therefore, it is critical to develop ultrasensitive electrochemical methods for sensitive detection of CTCs. To improve the sensitivity of the electrochemical method, our group combined rolling circle amplification (RCA) strategy with DNA generated electrochemical current technique for signal amplification [12]. The reaction of DNA, especially, the reaction of phosphate backbone of DNA with molybdate, can form redox molybdophosphate and generate electrochemical current [13–15].

Recently, two-dimensional semiconductor nanomaterials have provoked considerable interest owing to their prominent structures and physicochemical properties [16–18]. Their layered structures, and excellent electronic and optical characteristics make them attractive candidates in many biomedical areas [19, 20]. Among them, black phosphorus (BP) has become a research hotspot in the fields of electronic and optoelectronic chemistry due to its impressive carrier mobility [21]. Besides, it can be used as a supporting matrix to immobilize sensing materials for biosensing applications due to its large surface area [22]. However, BP has intrinsic limitations, such as poor stability in air-exposed water environments, which prevents its practical applications [23]. It has been

Electronic supplementary material The online version of this article (https://doi.org/10.1007/s00604-020-04367-8) contains supplementary material, which is available to authorized users.

✉ Minghui Yang
yangminghui@csu.edu.cn

[1] Hunan Provincial Key Laboratory of Micro & Nano Materials Interface Science, College of Chemistry and Chemical Engineering, Central South University, Changsha 410083, Hunan, People's Republic of China

Published online: 21 June 2020

reported that a pair of lone pairs of electrons in BP is exposed, which can react with oxygen to form PxOy species. PxOy species could be removed, and BP continues to be oxidized with degradation [24, 25]. Therefore, how to stabilize lone pairs of electrons needs to be solved for BP applications. A number of methods including covalent functionalization [26], noncovalent functionalization [27–29], and coordination with transitional metal ion have been developed to improve its stability [30, 31]. However, the stability-related limitation of BP still remains a challenge. In this mind, we synthesized gold nanoparticle–anchored BP nanosheets (BP@AuNPs) through in situ growth of AuNPs onto BP to stabilize BP. At the same time, PxOy species are produced and stabilized via the strong chelating ability of Au with PxOy species, which can generate electrochemical current after reaction with molybdate.

Herein, we reported the combination of magnetic nanobeads (MNs) and functionalized BP nanosheets for isolation and detection of CTCs with dual signal amplification strategy. Breast cancer cell MCF-7 cell was chosen as a model. The aptamer specific to MUC1 (overexpressed on MCF-7 cell surface) was immobilized on BP@AuNPs to form BP@AuNPs@aptamer, which was used as an electrochemical signal probe. According to our previous report, the PxOy species on BP and aptamer can both react with molybdate to form redox molybdophosphate and generate an electrochemical current, leading to dual signal amplification [32, 33]. The dual signal amplification improved the sensitivity of electrochemical detection. And the magnetic nanobeads modified with antiepithelial cell adhesion molecule (EpCAM) antibody enabled efficient enrichment and separation of MCF-7 cells. The proposed highly sensitive, selective sensor through combining functionalized BP nanosheets and immunomagnetic nanobeads was demonstrated to work well for CTC detection in human blood.

Experimental section

Materials and reagents

BP powder was purchased from HWRK Chemicals (Beijing, China, http://www.hwrkchemical.com/) and stored in a dark Ar glovebox. *N*-Methyl-2-pyrrolidone (NMP), sodium molybdate dihydrate (Na_2MoO_4•$2H_2O$), 1-ethyl-3-(3-dimethylaminopropyl) carbodiimide (EDC), *N*-hydroxysuccinimide (NHS), and propidium iodide (PI) were purchased from Sigma-Aldrich (St. Louis, MO, https://www.sigmaaldrich.com). Gold chloride tetrahydrate ($HAuCl_4$·$4H_2O$) was obtained from Sangon Biotech Co., Ltd. (Shanghai, China, https://www.sangon.com/). The aptamer with a sequence of 5′-SH-CACTACAGAGGTTG CGTCTGTCCCACGTTGTCATGGGGGGTTGGCCTG was synthesized and purified by Sangon Biotech Co., Ltd. (Shanghai, China, https://www.sangon.com/). EpCAM-antibody was obtained from Abcam Co., Ltd. (Cambridge, MA, https://www.abcam.cn). Polyacrylic acid (PAA), iron chloride hexahydrate ($FeCl_3$·$6H_2O$), sodium acetate anhydrous (CH_3COONa), and ethanediol (EG) were bought from Macklin (Shanghai, China, http://www.macklin.cn). SYTO 9 green-fluorescent nucleic acid stain (SYTO-9) was bought from Thermo Fisher (https://www.thermofisher.com). The living MCF-7, HeLa cell, and normal whole blood were obtained from Xiangya Hospital. All solutions were prepared using deionized water.

Apparatus and instruments

The size and morphology of the nanomaterials were characterized by scanning electron microscopy (SEM, EOL JSM-6700) and transmission electron microscopy (TEM, FEI Titan G2 60-300). An atomic force microscope (AFM, NanoManVS) was used to evaluate the morphology and height of BP nanosheets. Zeta potential and dynamic light scattering (DLS) were measured on the Malvern Zetasizer Nano (ZEN3600). UV-Vis absorption spectra was measured with a spectrophotometer (UV-2450). A microplate reader (ELX800) was used to perform cell vitality. X-Ray diffraction (XRD) analysis was carried out on a X-ray diffractometer (Pert PRO). X-Ray photoelectron spectroscopy (XPS) was carried out with a X-ray photoelectron spectrometer (Thermo Scientific K-Alpha+). The intracellular fluorescence imaging was carried out on an inverted fluorescence microscope (IX 83). All the electrochemical measurements were performed with an electrochemical workstation (CHI-650D). A standard three-electrode system consisting of a magnetic glassy carbon electrode (MGCE, 3 mm in diameter), a saturated Ag/AgCl reference electrode, and a platinum auxiliary electrode was used in all the electrochemical measurements.

Synthesis of BP nanosheets

BP nanosheets were synthesized from BP powder by liquid exfoliation [34]. In a typical procedure, BP powder was added into NMP (2 mg mL^{-1}) and sonicated for 10 h in an ice bath. After that, the solution was centrifuged at 3000 rpm for 10 min to remove the residue, and the supernatant was collected. The supernatant was further centrifuged at 12,000 rpm for 10 min to obtain precipitate as BP nanosheets.

Preparation of BP@AuNPs@aptamer

The BP@AuNP nanohybrids were synthesized through in situ ultrasonic synthesis. In brief, 30 μL $HAuCl_4$ solution (10 mM) was added into 0.5 mL of BP nanosheets (400 μg mL^{-1}) and sonicated for 10 min. The solution was centrifuged at 10,000 rpm for 10 min and washed twice with

deionized water. Subsequently, aptamer was added in BP@AuNP nanohybrids solution and shaken overnight at 4 °C. After another round of centrifugation, the final product was re-dispersed in deionized water and stored in a 4 °C refrigerator.

Synthesis of MNs and functionalization of MNs with anti-EpCAM

According to previous literature report, MNs with carboxyl group–terminated surfaces were synthesized by a solvothermal method [35]. In brief, 1.35 g $FeCl_3 \cdot 6H_2O$, 3.2 g CH_3COONa, and 0.5 mL PAA were dissolved in 38 mL EG and sonicated for 15 min. Then, the mixture solution was transferred into a 100 mL autoclave and heated for 6 h at 473 K. After magnetic separation, the solution was washed three times with ethanol alternately and deionized water and dried in a vacuum drying oven at 373 K to obtain carboxyl group–modified MNs.

The anti-EpCAM antibody was fixed onto the MNs by carbodiimide chemistry. Firstly, 7.5 mg MNs were dissolved in 1.5 mL of PBS (0.01 M, pH = 6.8) with 75 mM EDC and 75 mM NHS. The mixture was sonicated for 15 s and shaken for 20 min at room temperature. Then, MNs were separated magnetically, washed three times with PBS (0.01 M, pH = 7.2), and re-dispersed in 1 mL of PBS (0.01 M, pH = 7.2). After that, anti-EpCAM antibody was added into MNs solution at a concentration of 75 μg mL^{-1} and incubated for 4 h under continuous shaking at room temperature. Finally, the product was washed with deionized water to remove unmodified anti-EpCAM antibody and resuspended in 1 mL of deionized water. To block nonspecific sites on the MNs, 1% BSA was added to solutions for 30 min before each use.

Cell culture and capture

MCF-7 and HeLa cells were cultured in 1640 medium supplemented with 10% fetal bovine serum, penicillin (100 U mL^{-1}), and streptomycin (0.1 mg mL^{-1}) at 37 °C in a humidified atmosphere containing 5% CO_2.

For the cell capture, first, 100 μL anti-EpCAM-MNs (100 μg mL^{-1} MNs) were added into different concentrations of cell solution (1 mL) and shaken for 1 h at room temperature. Then, the enriched cells were separated with a magnet and washed three times with saline (0.9% NaCl). Finally, the MNs with captured cells were dispersed into 30 μL solution.

Cytotoxicity study

Cytotoxicity of anti-EpCAM-MNs and BP@AuNPs@aptamer was tested with a CCK-8 assay kit. First, 1×10^4 MCF-7 cells were added into a 96-well plate and incubated for 24 h; then, different concentrations of anti-EpCAM-MNs and BP@AuNPs@aptamer were added. After incubation for 24 h, CCK-8 reagent solution was added for another 2 h and cell viability was measured.

Fabrication of electrochemical biosensor

First, MNs captured with different amounts of cells were dropped onto the cleaned MGCE and left at room temperature. After washing, 10 μL BP@AuNPs@aptamer probe was added onto the electrode for 1 h at room temperature. Then, the modified electrode was washed and dried with nitrogen. Finally, 10 μL 5 mM Na_2MoO_4 was added onto the prepared electrode and incubated for 25 min at 37 °C. The electrochemical signal was measured in 0.5 M H_2SO_4.

Results and discussion

Principle of the biosensor

In order to develop a sensitive biosensor for MCF-7 cell detection, we utilized anti-EpCAM-MNs as a capture probe and AuNPs-functionalized BP nanosheets as an electrochemical signal probe. The AuNPs anchored on BP nanosheets improved the stability of the BP nanosheets. Scheme 1 schematically illustrates the biosensor preparation and measuring principle. For the synthesis of the signal probe, BP@AuNP nanohybrids were synthesized by in situ growth method to deposit AuNPs onto a BP nanosheets surface. The aptamer was then attached to the surface of BP@AuNP nanosheets by Au–S bond to form an aptamer-modified signal probe. Anti-EpCAM antibody–modified MNs were utilized to capture and enrich MCF-7 cells from complex sample due to the expression of EpCAM on the MCF-7 cell surface. After the anti-EpCAM-MNs with captured cells were immobilized onto the MGCE surface, the signal probe was further assembled onto the electrode through binding between aptamer and MUC1 that expressed on the MCF-7 cell surface to form the sandwich-type structure. Finally, the dual current generated by the reaction between PxOy species on aptamer backbone and BP nanosheets surface with Na_2MoO_4 was measured.

Synthesis and characterization of BP@AuNP nanohybrids

The BP nanosheets were synthesized by a liquid exfoliating method. The TEM image of the prepared BP nanosheets shows an average diameter of around 250 nm (Fig. 1A). The AFM image displays that the thickness of BP nanosheets is about 5.5 nm (Figure S1). The BP@AuNP nanohybrids were prepared by in situ growth

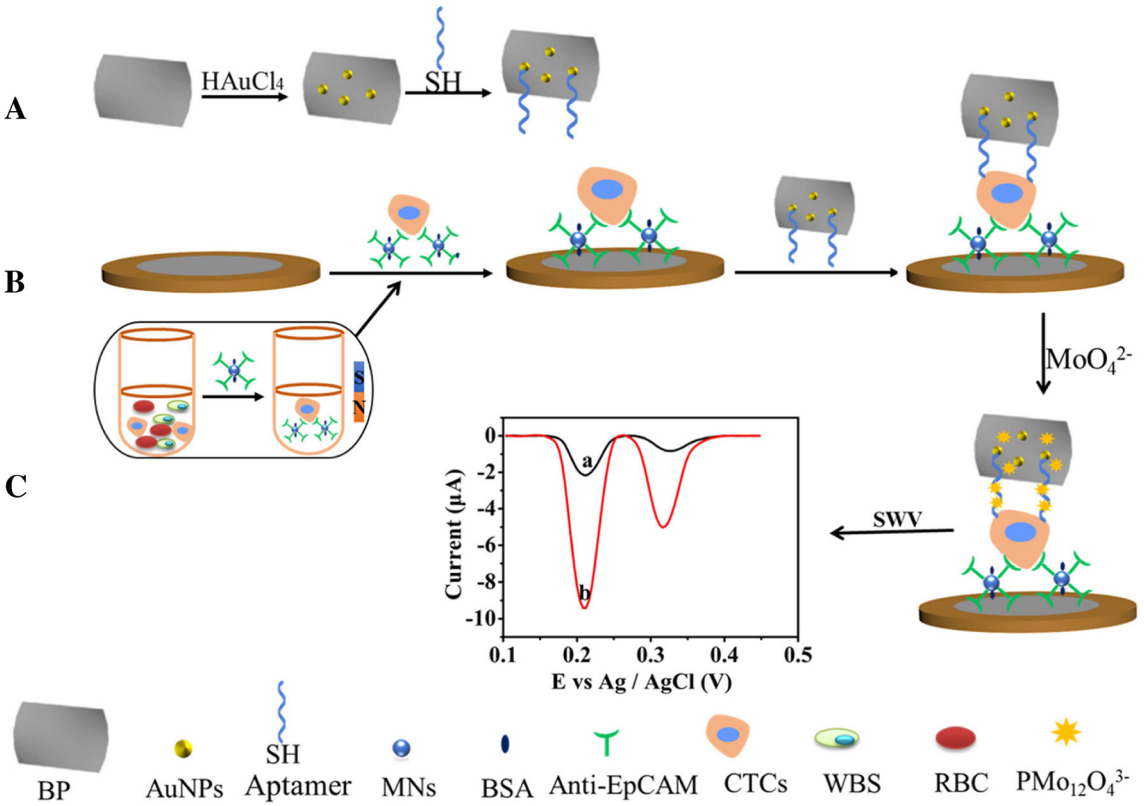

Scheme 1 Schematic illustration of the electrochemical sensor for cell capture and detection through the combination of BP@AuNPs@aptamer and anti-EpCAM-MNs. (A) Preparation of signal probe. (B) Preparation of the sandwich-type sensor. (C) Generation of dual electrochemical signal

method with the help of ultrasound. The TEM image of BP@AuNP nanohybrids reveals that AuNPs were well distributed on the BP nanosheets (Fig. 1B). The HRTEM image exhibits spacing of the crystal lattice fringes as 0.235 nm corresponding to the (111) plane of pure AuNPs (Fig. 1C). The crystal structure and chemical composition of BP@AuNP nanohybrids were also examined by XRD and XPS. The XRD patterns show that all diffraction peaks of BP@AuNP nanohybrids can be indexed into P and Au, which are consistent with JCPDS 76-1957 and JCPDS 04-0784, respectively (Figure S2). As presented in Fig. 1D, for the XPS spectrum of BP@AuNP nanohybrids, the crystalline BP nanosheets show two characteristic peaks with bands at 128.6 and 129.5 eV, corresponding to P $2p_{3/2}$ and P $2p_{1/2}$, respectively. Besides, sub-bands corresponding to PxOy species are evident at 132.6 eV, which have been studied in a previous report [36]. The existence of Au can be proved by the bands of 83.8 eV and 87.6 eV. The formation mechanism of AuNPs on BP nanosheets is likely due to the redox reaction between BP nanosheets and $HAuCl_4$. The redox potential of $AuCl_4^-/Au^0$ (+0.93 V) is higher than that of BP nanosheets (+0.21 V), allowing spontaneous electron transfer from BP nanosheets to $HAuCl_4$, resulting in the formation of AuNPs and concomitant with the production of the PxOy species. In addition, the peak of PxOy species is enhanced from the XPS spectrum, further indicating the occurrence of the reaction. Due to the strong chelating ability of P or PxOy species with AuNPs [37], the formation of AuNPs on BP nanosheets improved the stability of BP nanosheets. This is proved by the redshift of the binding energy bands of BP (Fig. 1D) because of the formation of the P–Au/P–O–Au bond. In addition, the increased PxOy species can be used to generate an electrochemical signal.

Successful preparation of the BP@AuNP nanohybrids and BP@AuNPs@aptamer can be further proved by UV-Vis absorption spectroscopy and zeta potential analysis. As shown in Fig. 1E, BP nanosheets (curve a) show no absorption peak whereas BP@AuNP nanohybrids (curve b) present a strong peak with a maximum absorption wavelength of 525 nm. After combining with aptamer, absorption peak intensity is decreased slightly and the position of maximum absorption is redshifted by 2 nm. Zeta potential analysis is shown in Fig. 1F; with the successful modification of AuNPs and aptamer onto the BP nanosheets, the zeta potential decreases correspondingly, indicating change of surface charge during the BP nanosheets modification process. The above characterization results demonstrated the successful modification of AuNPs and aptamer onto BP nanosheets.

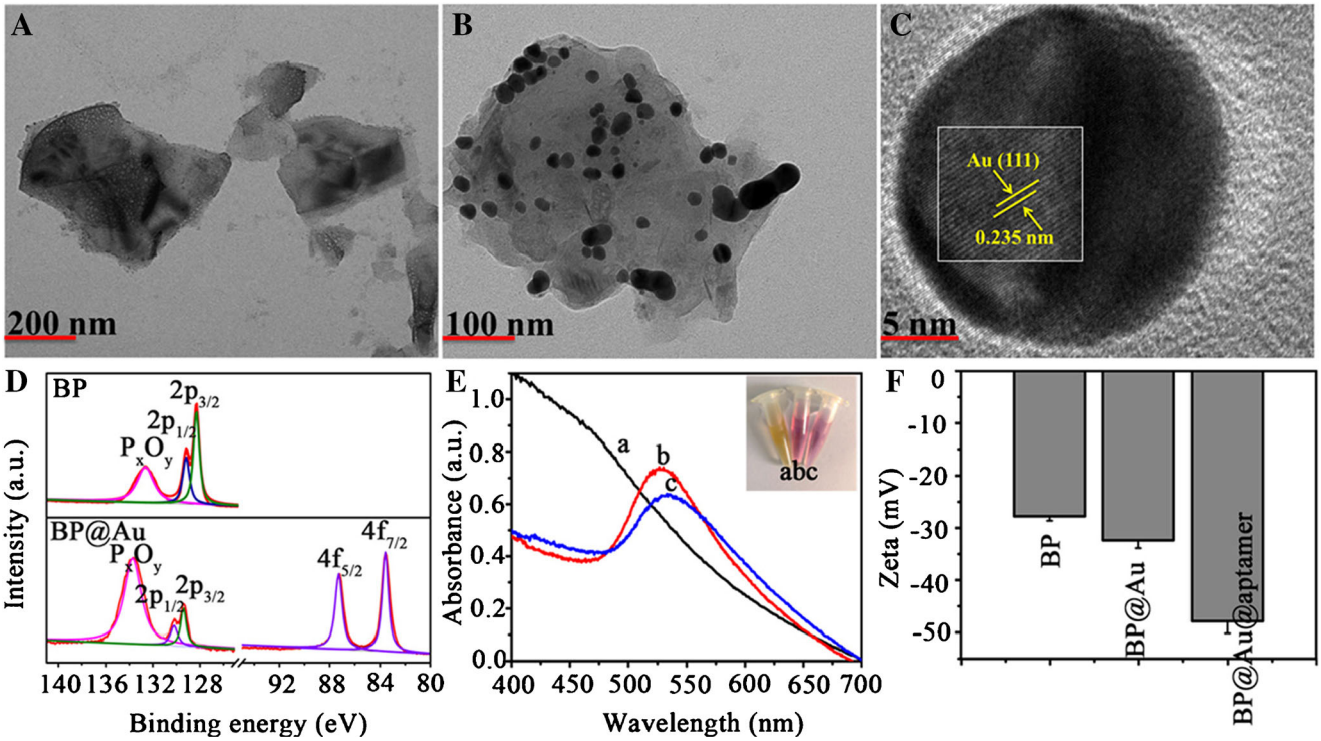

Fig. 1 (A) TEM images of BP nanosheets. (B) TEM images of BP@AuNP nanohybrids. (C) HRTEM image of BP@AuNP nanohybrids. (D) XPS spectra of BP nanosheets and BP@AuNP nanohybrids. (E) UV-Vis spectral analysis, (a) BP nanosheets, (b) BP@AuNP nanohybrids, (c) BP@AuNPs@aptamer. The inset shows digital photos of the corresponding solutions. (F) Zeta potential characterization

Characterization of MNs and anti-EpCAM-MN probe

The MNs with the carboxyl group were synthesized by the hydrothermal method. The morphology of MNs was characterized with SEM. As shown in Fig. 2A, the SEM image of MNs displays spherically shaped particles of about 200 nm. The anti-EpCAM antibody was linked to the MNs through linking between carboxyl group of MNs and amino group of antibodies. The result of the bonding reaction is reflected by DLS analysis. As shown in Fig. 2B, the size of anti-EpCAM-MNs is larger compared with that of bare MNs, which is attributed to the conjugation of antibodies onto MNs.

In vitro assessment

To demonstrate the possibility of the anti-EpCAM-MNs and BP@AuNPs@aptamer probes for the in vitro sample, we performed a series of in vitro experiments. Cells with and without

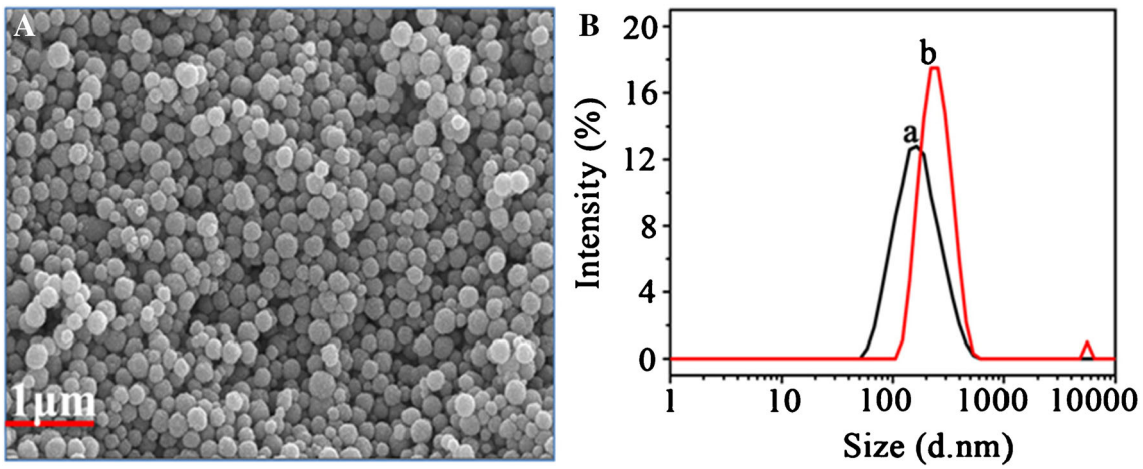

Fig. 2 Characterization of MNs and the anti-EpCAM-MNs probe. (A) SEM image of MNs. (B) The size distribution of MNs before (a) and after (b) anti-EpCAM conjugation

interaction with these probes were co-incubated in the incubator for 2 h and stained with PI and STYO-9, two widely used cell viability indicators. The morphology of the cells was observed using a fluorescence microscope (Figure S3). The microscopic bright-field images show that cell surface adhered to a great deal of probes through the membrane. And the stained cell with and without probes was kept still alive. These results proved that the probes have low toxicity and good affinity for MCF-7 cells that can be used to identify MCF-7 cells. Moreover, cell viability was also determined by CCK-8 kit to evaluate the cytotoxicity of probes. As shown in Figure S4, low toxicity of our probe was observed even at a high dose of 100 μg mL^{-1} (anti-EpCAM-MNs) and 400 μg mL^{-1} (BP@AuNPs@aptamer), revealing its promise in real application of synthetic probes with good biocompatibility and low cytotoxicity.

Electrochemical activity of the BP@AuNPs@aptamer probe

The electrochemical activity of the BP@AuNPs@aptamer probe was studied via cyclic voltammetry (CV). The aptamer, BP@AuNP nanohybrids, and BP@AuNPs@aptamer were directly immobilized onto the MGCE and then reacted with sodium molybdate. As shown in Fig. 3, for the aptamer-modified electrode, a pair of relatively small redox current is observed at around 0.22 and 0.37 V (curve b). The generated electrochemical current is caused by the reaction of phosphate backbone of aptamer molecule with molybdate to produce molybdophosphate precipitation. Similarly, for the BP@AuNP nanohybrids–modified electrode, peak current and peak position are similar to aptamer-modified electrode (curve c). The generated current can be attributed to PxOy on BP nanosheets. Using BP nanosheets as supporting matrix can not only increase the load of AuNPs due to the large surface area but also produce PxOy species with the help of $HAuCl_4$, generating current signal. Compared with BP@AuNP nanohybrids and aptamer-modified electrode, it can be seen that the redox current of BP@AuNPs@aptamer-modified electrode is enhanced about 2 times (curve d). The result proved that the aptamer was successfully conjugated onto AuNPs, leading to enhanced current intensity.

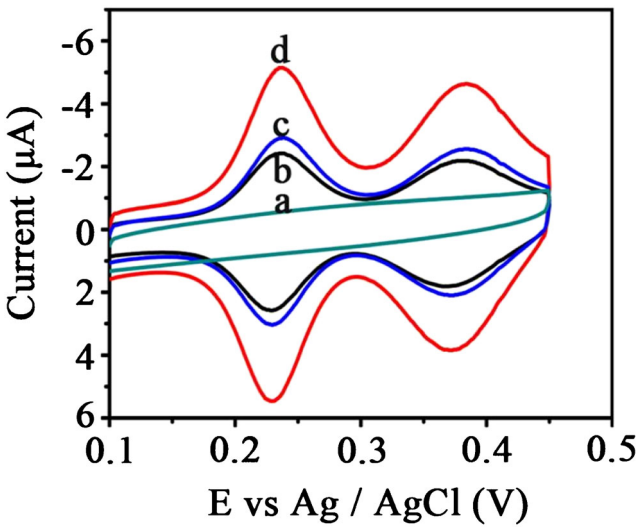

Fig. 3 CV responses of the different electrodes. (a) Bare electrode, (b) aptamer-modified electrode, (c) BP@AuNP nanohybrids–modified electrode, (d) BP@ AuNPs @aptamer–modified electrode

Feasibility of the proposed method

To prove the feasibility of the biosensor for MCF-7 cell detection, CV and square wave voltammetry (SWV) tests were performed. As shown in Fig. 4A, there is a pair of small redox current for blank sample detection with proposed biosensor (curve b) when compared with bare electrode (curve a), which may be attributed to the aptamer nonspecifically adsorbed onto the electrode. For detection of 1000 cell mL^{-1} MCF-7 cells, the current intensity of the biosensor is increased significantly. Especially, the current intensity is increased more significantly when using BP@AuNPs@aptamer as the signal probe instead of just using aptamer as the signal probe. Besides, the CV results were further confirmed by SWV characterization. As shown in Fig. 4B, the peak current intensity of the biosensor at 0.22 V is enhanced about 2.5 times compared with that of the biosensor using aptamer as the signal probe. These data proved the possibility of the sensor for cell detection. What's more, these results also demonstrated the dual signal amplification strategy due to BP and aptamer can significantly enhance the sensitivity of the biosensor.

Performance of the biosensor

To explore the ability of the sensor for MCF-7 cell–sensitive quantification, the sensor was tested with different concentrations of MCF-7 cells. Figure 4C displays SWV responses of the sensor to seven concentrations of MCF-7 cells in the range from 0 to 1000 cell mL^{-1}. As can be seen from the figure, the current intensity at about 0.2 V is increased along with the increasing MCF-7 cell concentration. A linear relationship between the change of current intensity and logarithm of MCF-7 cell concentration was obtained from 10 to 1000 cell mL^{-1} with a linear correlation coefficient of 0.99. The detection limit is thus estimated to be 2 cell mL^{-1} (S/N = 3).

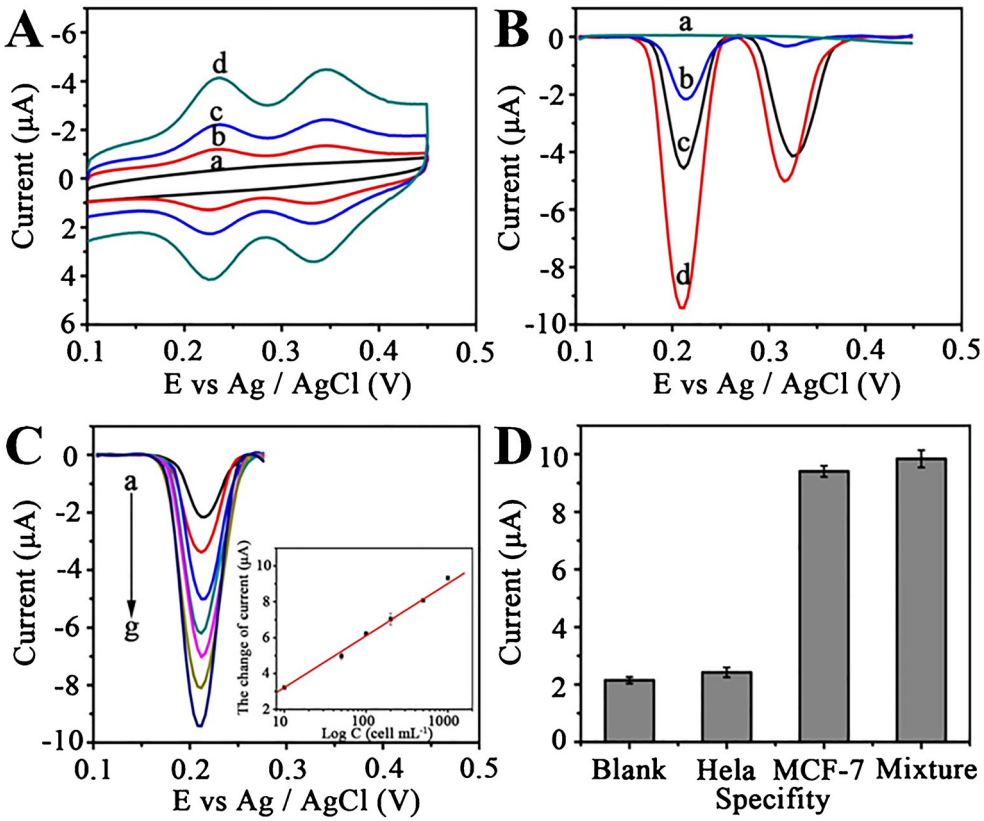

Fig. 4 (A) CV responses of the different sensor after reaction with molybdate in 0.5 M H_2SO_4, (a) bare electrode, (b) sensor for 0 cell mL^{-1}, (c) sensor for 1000 cell mL^{-1} with aptamer as the signal probe, (d) sensor for 1000 cell mL^{-1} with BP@AuNPs@aptamer as the signal probe. (B) The corresponding SWV responses of the sensors. (C) SWV responses of the electrochemical sensor to different concentrations of MCF-7 from (a) to (g): 0, 10, 100, 200, 500, 1000 cell mL^{-1}. The inset shows the calibration curve of the sensor to MCF-7. (D) Specificity of the proposed sensor. Error bars = RSD ($n = 3$)

Furthermore, Table S1 shows the comparisons of different methods for the determination of cancer cells. It was worth pointing out that the detection limit of this sensor was better than that of other biosensors reported in literature.

Sensor selectivity and reproducibility

Selectivity is one of the important characteristics of biosensor, which represents the possibility of the sensor for the response to target substance over other substances (interfering substances). To evaluate the selectivity of our sensor toward MCF-7 cells, the current responses of HeLa cells and mixture solution of HeLa cell and MCF-7 cells were investigated. As shown in Fig. 4D, compared with blank sample, no remarkable current change toward 1000 cell mL^{-1} of HeLa cells was observed. However, when the same concentration of MCF-7 cells was detected, the current change was obvious. Moreover, the current change toward mixture solution (1000 cell mL^{-1} of HeLa cells with 1000 cell mL^{-1} of MCF-7 cells) was almost unchanged compared with the sample containing only 1000 cell mL^{-1} of MCF-7 cells. The result strongly demonstrates good selectivity of the sensor.

The reproducibility of the sensor was assessed by detecting the same samples with three modified electrodes. The relative standard deviation (RSD) of sensor to 100 cell mL^{-1} and 1000 cell mL^{-1} MCF-7 of cells were 1.81% and 1.27%, respectively, which suggests acceptable reproducibility of the method.

Detection of the blood samples

To further validate the reliability of the biosensor for clinical sample detection, the proposed sensor was applied to determine MCF-7 cells in whole blood. The MCF-7 cells were added into whole blood with concentrations of 30, 60, and 600 cell mL^{-1}. It can be seen that the determined results were

Table 1 Determination of MCF-7 cell added in human blood with the proposed sensor

Spiked (cell mL^{-1})	Detected (cell mL^{-1})	Mean (cell mL^{-1})	Recovery (%)	RSD (%)
30	31, 27, 32, 28, 30	30	100	6.9
60	61, 60, 60, 55, 61	59	98.3	4.2
600	596, 604, 601, 596, 597	599	99.8	0.59

highly in accordance with spiked amounts of MCF-7 cells (Table 1). The obtained recovery rates were in the range of 98.3–100%. This indicates that the developed sensor platform could be used for highly efficient detection of CTCs in real samples.

Conclusions

In summary, an ultrasensitive sandwich-like biosensor based on anti-EpCAM-MNs and BP@AuNPs@aptamer was successfully prepared and applied for highly efficient capture and sensitive detection of CTCs in whole blood. The anti-EpCAM-MNs was used as the capture probe to enrich and isolate CTCs by integrating strong magnetic properties of MNs as well as the high specificity of antibody. BP@AuNPs@aptamer was used as the signal probe to generate electrochemical current due to reaction of both BP and aptamer with molybdate. Experimental results proved that the developed sensor possesses high sensitivity with a low detection limit of 2 cell mL^{-1}, selectivity, and reproducibility for CTC detection. Besides, the sensor was successfully applied for detection of CTCs in peripheral blood samples without any blood sample pretreatment. Thus, the sensor provides promising possibilities for further clinical applications for cancer diagnosis and therapeutics. In addition, the signal amplification strategy can also find applications in various electrochemical assays.

Funding information This work was supported by the Hunan Provincial Science and Technology Plan Project, China (No. 2019TP1001), and Innovation-Driven Project of Central South University (2020CX002).

Compliance with ethical standards

Conflict of interest The authors declare that they have no competing interests.

References

1. Siegel RL, Miller KD, Jemal A (2015) Cancer statistics, 2015. CA-Cancer J Clin 65(1):5–29
2. Wan Y, Zhou Y-G, Poudineh M, Safaei TS, Mohamadi RM, Sargent EH, Kelley SO (2014) Highly specific electrochemical analysis of cancer cells using multi-nanoparticle labeling. Angew Chem Int Ed 53(48):13145–13149
3. Tang S, Shen H, Hao Y, Huang Z, Tao Y, Peng Y, Guo Y, Xie G, Feng W (2018) A novel cytosensor based on Pt@Ag nanoflowers and AuNPs/Acetylene black for ultrasensitive and highly specific detection of circulating tumor cells. Biosens Bioelectron 104:72–78
4. Zhou W, Gao X, Liu D, Chen X (2015) Gold nanoparticles for in vitro diagnostics. Chem Rev 115(19):10575–10636
5. Gu Y, Ju C, Li Y, Shang Z, Wu Y, Jia Y, Niu Y (2015) Detection of circulating tumor cells in prostate cancer based on carboxylated graphene oxide modified light addressable potentiometric sensor. Biosens Bioelectron 66:24–31
6. Hou J-M, Krebs M, Ward T, Sloane R, Priest L, Hughes A, Clack G, Ranson M, Blackhall F, Dive C (2011) Circulating tumor cells as a window on metastasis biology in lung cancer. Am J Pathol 178(3):989–996
7. Warkiani ME, Guan G, Luan KB, Lee WC, Bhagat AA, Chaudhuri PK, Tan DS, Lim WT, Lee SC, Chen PC, Lim CT, Han J (2014) Slanted spiral microfluidics for the ultra-fast, label-free isolation of circulating tumor cells. Lab Chip 14(1):128–137
8. Wang X, Xia J, Wang C, Liu L, Zhu S, Feng W, Li L (2017) Preparation of novel fluorescent nanocomposites based on Au nanoclusters and their application in targeted detection of cancer cells. ACS Appl Mater Interfaces 9(51):44856–44863
9. Sawada T, Watanabe M, Fujimura Y, Yagishita S, Shimoyama T, Maeda Y, Kanda S, Yunokawa M, Tamura K, Tamura T, Minami H, Koh Y, Koizumi F (2016) Sensitive cytometry based system for enumeration, capture and analysis of gene mutations of circulating tumor cells. Cancer Sci 107(3):307–314
10. Wang H, Zhou C, Sun X, Jian Y, Kong Q, Cui K, Ge S, Yu J (2018) Polyhedral-AuPd nanoparticles-based dual-mode cytosensor with turn on enable signal for highly sensitive cell evalution on lab-on-paper device. Biosens Bioelectron 117:651–658
11. Han S-I, Han K-H (2015) Electrical detection method for circulating tumor cells using graphene nanoplates. Anal Chem 87(20): 10585–10592
12. Shen C, Liu S, Li X, Yang M (2019) Electrochemical detection of circulating tumor cells based on DNA generated electrochemical current and rolling circle amplification. Anal Chem 91(18): 11614–11619
13. Cao S, Wang Q, Xiao X, Li T, Yang M (2019) Electrochemical immunoassay for the tumor marker CD25 by coupling magnetic sphere-based enrichment and DNA based signal amplification. Microchim Acta 186(6):352–356
14. Liu S, Jiang X, Yang M (2019) Electrochemical sensing of L-ascorbic acid by using a glassy carbon electrode modified with a molybdophosphate film. Microchim Acta 186(7):445–451
15. Jiang X, Liu S, Yang M, Rasooly A (2019) Amperometric genosensor for culture independent bacterial count. Sens Actuators B Chem 299:126944–126949
16. Chen W, Ouyang J, Yi X, Xu Y, Niu C, Zhang W, Wang L, Sheng J, Deng L, Liu Y-N, Guo S (2018) Black phosphorus nanosheets as a neuroprotective nanomedicine for neurodegenerative disorder therapy. Adv Mater 30(3):1703458–1703464
17. Chhowalla M, Jena D, Zhang H (2016) Two-dimensional semiconductors for transistors. Nat Rev Mater 1(11):16052–16066
18. Song G, Hao J, Liang C, Liu T, Gao M, Cheng L, Hu J, Liu Z (2016) Degradable molybdenum oxide nanosheets with rapid clearance and efficient tumor homing capabilities as a therapeutic nanoplatform. Angew Chem Int Ed 55(6):2122–2126
19. Gong L, Yan L, Zhou R, Xie J, Wu W, Gu Z (2017) Two-dimensional transition metal dichalcogenide nanomaterials for combination cancer therapy. J Mater Chem B 5(10):1873–1895
20. Tan C, Cao X, Wu X-J, He Q, Yang J, Zhang X, Chen J, Zhao W, Han S, Nam G-H, Sindoro M, Zhang H (2017) Recent advances in ultrathin two-dimensional nanomaterials. Chem Rev 117(9):6225–6331
21. Wang H, Yang X, Shao W, Chen S, Xie J, Zhang X, Wang J, Xie Y (2015) Ultrathin black phosphorus nanosheets for efficient singlet oxygen generation. J Am Chem Soc 137(35):11376–11382
22. Peng J, Lai Y, Chen Y, Xu J, Sun L, Weng J (2017) Sensitive detection of carcinoembryonic antigen using stability-limited few-layer black phosphorus as an electron donor and a reservoir. Small 13(15):1603588–1603598
23. Liu G, Tsai H-I, Zeng X, Qi J, Luo M, Wang X, Mei L, Deng W (2019) Black phosphorus nanosheets-based stable drug delivery

system via drug-self-stabilization for combined photothermal and chemo cancer therapy. ChemEngJ 375:121917–121916
24. Favron A, Gaufres E, Fossard F, Phaneuf-L'Heureux AL, Tang NY, Levesque PL, Loiseau A, Leonelli R, Francoeur S, Martel R (2015) Photooxidation and quantum confinement effects in exfoliated black phosphorus. Nat Mater 14(8):826–832
25. Ling X, Wang H, Huang S, Xia F, Dresselhaus MS (2015) The renaissance of black phosphorus. Proc Natl Acad Sci U S A 112(15):4523–4530
26. Ryder CR, Wood JD, Wells SA, Yang Y, Jariwala D, Marks TJ, Schatz GC, Hersam MC (2016) Covalent functionalization and passivation of exfoliated black phosphorus via aryl diazonium chemistry. Nat Chem 8(6):597–602
27. Abellán G, Lloret V, Mundloch U, Marcia M, Neiss C, Görling A, Varela M, Hauke F, Hirsch A (2016) Noncovalent functionalization of black phosphorus. Angew Chem Int Ed 55(47):14557–14562
28. Korolkov VV, Timokhin IG, Haubrichs R, Smith EF, Yang L, Yang S, Champness NR, Schroder M, Beton PH (2017) Supramolecular networks stabilise and functionalise black phosphorus. Nat Commun 8(1):1385–1392
29. Zeng X, Luo M, Liu G, Wang X, Tao W, Lin Y, Ji X, Nie L, Mei L (2018) Polydopamine-modified black phosphorous nanocapsule with enhanced stability and photothermal performance for tumor multimodal treatments. Adv Sci 5(10):1800510–1800517
30. Guo Z, Chen S, Wang Z, Yang Z, Liu F, Xu Y, Wang J, Yi Y, Zhang H, Liao L, Chu PK, Yu X-F (2017) Metal-ion-modified black phosphorus with enhanced stability and transistor performance. Adv Mater 29(42):1703811–1703818
31. Zhao Y, Wang H, Huang H, Xiao Q, Xu Y, Guo Z, Xie H, Shao J, Sun Z, Han W, Yu X-F, Li P, Chu PK (2016) Surface coordination of black phosphorus for robust air and water stability. Angew Chem Int Ed 55(16):5003–5007
32. Chai Y, Li X, Yang M (2019) Aptamer based determination of the cancer biomarker HER2 by using phosphate-functionalized MnO2 nanosheets as the electrochemical probe. Microchim Acta 186(5): 316–321
33. Wang G, Wang H, Cao S, Xiang W, Li T, Yang M (2019) Electrochemical determination of the activity and inhibition of telomerase based on the interaction of DNA with molybdate. Microchim Acta 186(2):96–101
34. Ouyang J, Deng L, Chen W, Sheng J, Liu Z, Wang L, Liu Y-N (2018) Two dimensional semiconductors for ultrasound-mediated cancer therapy: the case of black phosphorus nanosheets. Chem Comm 54(23):2874–2877
35. Zheng T, Zhang Q, Feng S, Zhu JJ, Wang Q, Wang H (2014) Robust nonenzymatic hybrid nanoelectrocatalysts for signal amplification toward ultrasensitive electrochemical cytosensing. J Am Chem Soc 136(6):2288–2291
36. Chen W, Ouyang J, Liu H, Chen M, Zeng K, Sheng J, Liu Z, Han Y, Wang L, Li J, Deng L, Liu YN, Guo S (2017) Black phosphorus nanosheet-based drug delivery system for synergistic photodynamic/photothermal/chemotherapy of cancer. Adv Mater 29(5): 1603864–1603870
37. Cano I, Chapman AM, Urakawa A, van Leeuwen PW (2014) Air-stable gold nanoparticles ligated by secondary phosphine oxides for the chemoselective hydrogenation of aldehydes: crucial role of the ligand. J Am Chem Soc 136(6):2520–2528